Spin-orbit coupling controlling the topological vortical phase transition in spin-2 rotating Bose-Einstein condensates

Hao Zhu [1,2] Chao-Fei Liu,[3,*] Deng-Shan Wang,[4] Shou-Gen Yin,[1,†] Lin Zhuang,[5,‡] and Wu-Ming Liu [2,6,7,§]

[1]*Key Laboratory of Display Materials and Photoelectric Devices (Ministry of Education), Tianjin Key Laboratory for Photoelectric Materials and Devices, School of Materials Science and Engineering, Tianjin University of Technology, Tianjin 300384, China*

[2]*Beijing National Laboratory for Condensed Matter Physics, Institute of Physics, Chinese Academy of Sciences, Beijing 100190, China*

[3]*School of Science, Jiangxi University of Science and Technology, Ganzhou 341000, China*

[4]*Laboratory of Mathematics and Complex Systems (Ministry of Education), School of Mathematical Sciences, Beijing Normal University, Beijing 100875, China*

[5]*School of Physics, Sun Yat-Sen University, Guangzhou 510257, China*

[6]*School of Physical Sciences, University of Chinese Academy of Sciences, Beijing 100190, China*

[7]*Songshan Lake Materials Laboratory, Dongguan, Guangdong 523808, China*

(Received 7 January 2021; accepted 9 November 2021; published 29 November 2021)

We investigate the combined effects of spin-orbit coupling and rotation on the topological vortical phase transition in $F = 2$ Bose-Einstein condensates. We find that the spin-orbit coupling can precisely manipulate the canonical atom current which is generated in the opposite direction of the gauge atom current and causes both a continuous and a discontinuous canonical angular momentum. We apply the canonical angular momentum and magnetization to reveal the emergence of novel topological excitations, such as the Anderson-Toulouse vortex as well as the vortex–dipole lattice. Especially, strong spin-orbit coupling can induce two perpendicular vortex chains. We also find that both the first-order and the second-order phase transition can be characterized by the canonical angular momentum and the magnetization. Differently from the spin singlet-pairing interaction, the spin-exchange interaction can adjust the canonical angular momentum and control the phase transition well. The topological vortical phase transition in an $F = 2$ cold-atom system is compatible with the current experiment and can be detected by the spin polarization procedure.

DOI: 10.1103/PhysRevA.104.053325

I. INTRODUCTION

Topological excitation in quantum fluid plays an important role in modern physics, ranging from quantum spin liquids [1] to superconductors [2] to nonrelativistic scales [3]. Among the plethora of physical systems, the highly controllable ultracold bosonic gases open a new path to engineering nontrivial excitation. The topological vortical phase transition has been widely investigated in Bose-Einstein condensates (BECs) [4] and various topological excitations have been theoretically predicted or experimentally observed, i.e., quantum vortices [5], bright solitons [6], and hopfions [7]. Since the quantized vortex was realized in scalar BECs [8,9], there has been growing interest in introducing the phase transition from the trivial phase in spinor BECs [10,11]. However, precisely regulating the phase transition remains a question.

Spin-orbit coupling (SOC) has attracted lots of attention in condensed matter systems, including spintronics [12] and topological insulators [13]. After Lin *et al.* realized SOC in ^{87}Rb atoms [14], Rashba-type or Dresselhaus-type SOC has been employed to manipulate the topological vortical phase transition [15,16]. Exotic SOC was theoretically predicted to trigger the plane-wave phase or stripe phase by Wang *et al.* [17], which enriched the phase diagram of spinor BECs [18,19]. On the other hand, rotation is one of the most common strategies to produce topological nontrivial states in spinor BECs [20,21]. Accompanied by the appearance of SOC, the rotation frequency Ω couples to the mechanical angular momentum operator $\hat{L}^{\text{mech}} = \hat{L}_z^c + \hat{L}_z^g$, with the canonical angular momentum operator $\hat{L}_z^c = -i\hbar(\hat{x}\hat{\partial}_y - \hat{y}\hat{\partial}_x)$ and gauge angular momentum operator $\hat{L}_z^g = m\lambda(\hat{x}\hat{\sigma}_x + \hat{y}\hat{\sigma}_y)$, where $\hat{\sigma}_{x,y}$ are Pauli matrices [22,23]. The combined effect of SOC and rotation facilitates the ground states to exhibit various topological structures in spin-1/2 or spin-1 BECs [24,25]. However, the more complicated spin-2 BECs offer an opportunity to trigger even more novel topological excitations, which has not been thoroughly investigated so far.

In this paper, we apply Rashba-type SOC to maneuver the topological vortical phase transition in spin-2 rotating BECs. Remarkably, an SOC-induced gauge atom current will excite the canonical atom current in the opposite direction. In the ground states of ferromagnetic BECs, the canonical angular momentum $\langle L_z^c \rangle$ is precisely regulated by SOC without rotation. Moreover, when considering the combined effect of SOC and rotation, the step-form changing magnetization $\mathcal{M}$ and $\langle L_z^c \rangle$ indicate new topological phases, including the

*liuchaofei@jxust.edu.cn
†sgyin@tjut.edu.cn
‡stszhl@mail.sysu.edu.cn
§wliu@iphy.ac.cn

Anderson-Toulouse (AT) vortex, the vortex-dipole lattice, and phase separation. Interestingly, extremely strong SOC can trigger two perpendicular vortex chains, which has not been reported in trapped spin-2 BECs before. We also discover that the spin-exchange interaction plays a more important role than the spin singlet-pairing interaction in the phase transition.

II. MODEL

We investigate the ground states of spin-2 BECs with SOC and rotation. In the mean-field approximation, the total Hamiltonian is defined as $H = H_0 + H_{\rm int}$ [26,27], in which the single-particle Hamiltonian H_0 becomes

$$\mathrm{H}_0 = \int d\boldsymbol{r}\boldsymbol{\psi}(\boldsymbol{r})^\dagger \left[\frac{\hat{p}^2}{2m} + \lambda(\hat{p}\cdot\hat{\sigma}_\mu) - \Omega\hat{L}_z^c + V(\boldsymbol{r})\right]\boldsymbol{\psi}(\boldsymbol{r}), \quad (1)$$

where $\boldsymbol{\psi} = (\psi_2, \psi_1, \psi_0, \psi_{-1}, \psi_{-2})^T$ characterizes the five-component order parameters. The total particle number is defined as $N = \int d\rho = \int \sum_{j=\pm2,\pm1,0} \psi_j{}^\dagger(\boldsymbol{r})\psi_j(\boldsymbol{r})$, m is the atomic mass, and $\boldsymbol{r} \equiv (x, y)$. The momentum $\hat{p} = -i\hbar\hat{\nabla}$, where $\hbar$ is the Planck constant. The projection of the angular momentum operator onto the z axis reads $\hat{L}_z^c$, $\hat{\sigma}_\mu$ $(\mu = x, y)$ are 5×5 spin-2 matrices, λ denotes the strength of the SOC, and Ω stands for the rotation frequency. The two-dimensional (2D) trapping potential is given by $V(\boldsymbol{r}) = \frac{1}{2}m\omega_\perp^2(x^2 + y^2)$, with $\omega_\perp$ denoting the oscillator frequencies along the x and y directions. It is convenient to make all quantities dimensionless by introducing a length scale $\xi_0 = \sqrt{\hbar/(m\omega_\perp)}$.

The interaction Hamiltonian $\mathrm{H}_{\rm int}$ is defined as

$$\begin{aligned}\mathrm{H}_{\rm int} = \frac{1}{2}\int d\boldsymbol{r}\big[&c_0\psi_i(\boldsymbol{r})^\dagger\psi_j(\boldsymbol{r})^\dagger\psi_j(\boldsymbol{r})\psi_i(\boldsymbol{r}) \\ &+ c_1\psi_i(\boldsymbol{r})^\dagger\psi_k(\boldsymbol{r})^\dagger\mathbf{F_{ij}}\cdot\mathbf{F_{kl}}\psi_l(\boldsymbol{r})\psi_j(\boldsymbol{r}) \\ &+ c_2(-1)^{i+j}\psi_i(\boldsymbol{r})^\dagger\psi_{-i}(\boldsymbol{r})\psi_j(\boldsymbol{r})^\dagger\psi_{-j}(\boldsymbol{r})\big], \quad (2)\end{aligned}$$

where $(\mathbf{F}_\mu)_{ij}$ $(\mu = x, y, z)$ are the (i, j) components of spin-2 matrices $\mathbf{F}_\mu$. $c_{0,1,2}$ represent the density-density interaction, spin-exchange interaction, and spin singlet-pairing interaction, respectively. With the aid of the imaginary-time method [28], the wave functions of ground states are obtained from the dimensionless coupled Gross-Pitaevskii equations [29,30], which are reported in the Appendix.

III. MANY-BODY GROUND STATES

A. Canonical atom current and gauge atom current

The condensate wave function $\boldsymbol{\psi}$ minimizes the Gross-Pitaevskii energy $H = H_0 + H_{\rm int}$. Depending on hydrodynamic theory, the mechanical movement contributes to the Hamiltonian as $H^{\rm mech} = \int \frac{m}{2\rho}(J_c + J_g)^2 dr$, where J_c represents the rotation-induced canonical atom current, and J_g represents the SOC-induced gauge atom current [31,32]. The canonical atomic current can generate the canonical angular momentum $\langle L_z^c\rangle = \sum_j \int \psi_j^\dagger[-i(x\nabla_y - y\nabla_x)]\psi_j dr$, where $j = \pm2, \pm1, 0$. With reference to Fig. 1(a), when SOC is absent, the canonical angular momentum does not respond to rotation until $\Omega = 0.2\omega_\perp$ (the clockwise J_c is indicated by the dark-red arrows in the inset). In the case $\Omega < 0.6\omega_\perp$, the $\langle L_z^c\rangle$-Ω curve increases linearly, but it increases exponentially

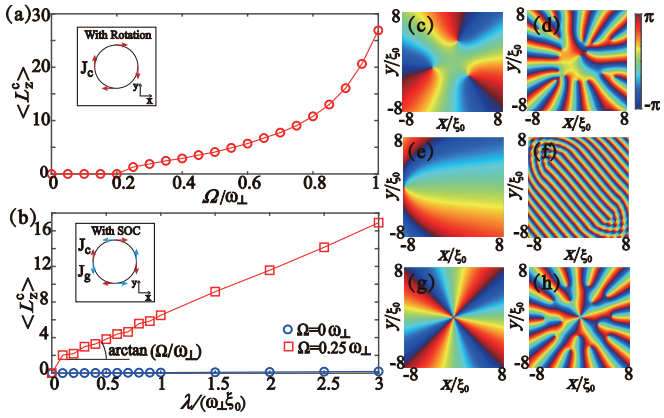

FIG. 1. (a) Evolution of the canonical angular momentum $\langle L_z^c\rangle$ with the rotation frequency Ω when SOC is absent. Inset: Dark-red arrows indicate the direction of the canonical atom current J_c. (b) Evolution of $\langle L_z^c\rangle$ with the SOC strength λ with $\Omega = 0$ and $0.25\omega_\perp$, respectively. Inset: Light-blue arrows indicate the gauge atom current J_g, which is in the opposite direction to the canonical atom current (dark red). (c)–(h) Phase field of the ψ_{-2} components for different λ and Ω, where $\Omega = 0.2\omega_\perp$, $\lambda = 0$ in (c), $\Omega = 0.5\omega_\perp$, $\lambda = 0$ in (d), $\Omega = 0$, $\lambda = 0.3\omega_\perp\xi_0$ in (e), $\Omega = 0$, $\lambda = 1.5\omega_\perp\xi_0$ in (f), $\Omega = 0.25\omega_\perp$, $\lambda = 0.3\omega_\perp\xi_0$ in (g), and $\Omega = 0.25\omega_\perp$, $\lambda = 1.5\omega_\perp\xi_0$ in (h). Spin-exchange interaction $c_1/c_0 = -0.008$, and spin singlet-pairing interaction $c_2/c_0 = 0.08$.

when $\Omega > 0.6\omega_\perp$. Characteristic density profiles of the ψ_{-2} component are depicted in Figs. 1(c) and 1(d), where the SOC strength $\lambda = 0$. When Ω is increased from 0 to $0.25\omega_\perp$, a typical axisymmetric vortex lattice replaces the vortex-free state, as depicted in Fig. 1(c). However, the symmetry of the vortex distribution is broken when Ω reaches $0.7\omega_\perp$ in Fig. 1(d). Obviously, pure rotation could induce vortex lattice in ferromagnetic spin-2 BECs. However, the irregular distribution of vortices makes it difficult to precisely manipulate the topological vortical phase transition.

Besides the canonical atom current, the gauge atom current, which is defined as $J_g = -\frac{1}{m}\psi^\dagger\mathbf{A}\psi$, with $\mathbf{A}$ defining the gauge potential, can also result in nontrivial vortex structures. For Rashba-type SOC, the gauge potential reads $\mathbf{A} = -\lambda m(\sigma_x, \sigma_y)$, leading to $J_g = \lambda\rho(F_x, F_y)$. In the presence of J_g, J_c is generated in the opposite direction [31] [as depicted by the inset in Fig. 1(b)], which means that SOC can also influence the canonical angular momentum $\langle L_z^c\rangle$. The evolution of $\langle L_z^c\rangle$ with the SOC strength λ is depicted in Fig. 1(b). Noticeably, the gradient of the $\langle L_z^c\rangle$-λ curve is approximately 0 when rotation is absent. This phenomenon can be explained by Figs. 1(e) and 1(f), where the SOC-induced vortices are distributed at the edge of the condensate, and the ground states are the plane-wave phase [17]. The angular momentum of these phase defects can be approximated as $\sim(1 - r^2/R^2)$ [33], where R is the size of the condensate and r is the distance from the vortex to the center, bearing in mind that the aforementioned vortices lie on the outskirts of the condensate ($r \sim R$) whose contribution to the angular momentum is negligible, equivalent to ghost vortices [34,35]. On the other hand, with the collaboration of SOC and rotation, the axisymmetric vortices contribute a nonnegligible angular momentum, as

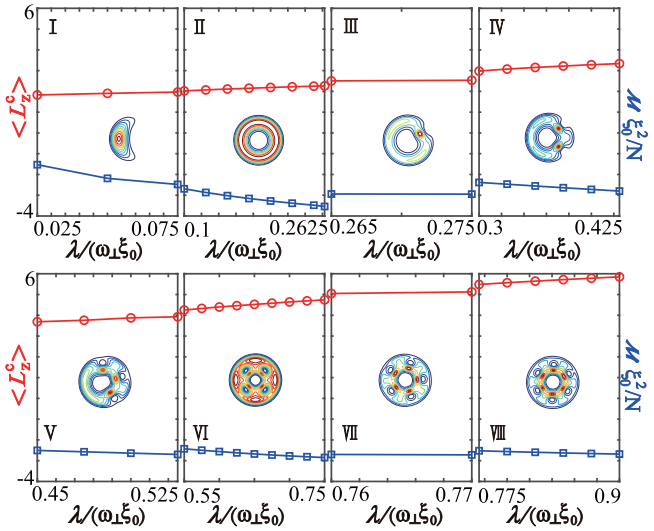

FIG. 2. Evolution of the canonical angular momentum $\langle L_z^c \rangle$ (red line with circles) and the magnetization $\mathcal{M}$ (blue line with rectangles), with the SOC strength λ ranging from 0 to $0.9\omega_\perp\xi_0$ and the rotation frequency fixed at $\Omega = 0.25\omega_\perp$. The density contours $|\psi_{-2}(\boldsymbol{r})|^2$ for $\lambda = 0.05\omega_\perp\xi_0$, $0.2\omega_\perp\xi_0$, $0.27\omega_\perp\xi_0$, $0.4\omega_\perp\xi_0$, $0.5\omega_\perp\xi_0$, $0.7\omega_\perp\xi_0$, $0.76\omega_\perp\xi_0$, and $0.85\omega_\perp\xi_0$ are labeled I–VIII, which indicate various topological excitations.

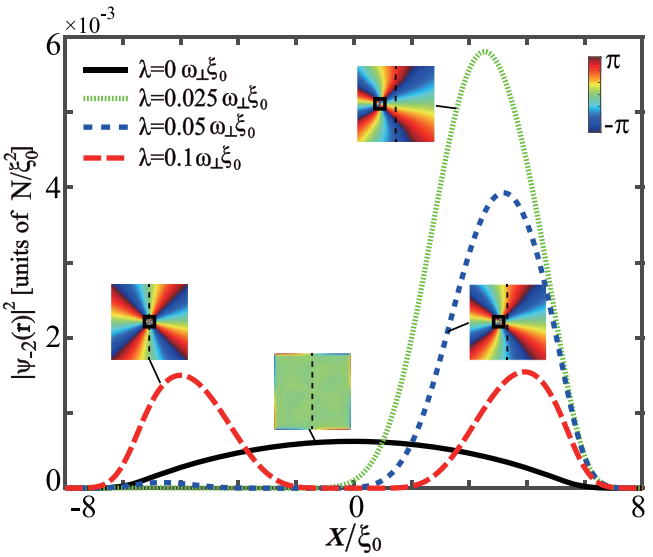

FIG. 3. The 1D density profile of the $\psi_{-2}(\boldsymbol{r})$ component with diverse SOC strengths λ, when the rotation frequency is fixed at $\Omega = 0.25\omega_\perp$. The corresponding phase field $\arg(\psi_{-2})$ indicates that the vortex core (represented by the black rectangle) is ultimately drawn back to the center of the cloud (represented by the dashed black line) when λ is tuned from $0 \to 0.1\omega_\perp\xi_0$.

shown in Figs. 1(g) and 1(h). Consequently, the gradient of the $\langle L_z^c \rangle$-λ curve can be approximated as $\arctan(\Omega/\omega_\perp)$ when $\Omega = 0.25\omega_\perp$.

B. First-order and second-order phase transitions

To determine the nature of the topological vortical phase transition, we first focus on the weakly spin-orbit-coupled BECs ($\lambda \leqslant 0.9\omega_\perp\xi_0$) when the rotation frequency remains stationary at $\Omega = 0.25\omega_\perp$. The canonical angular momentum $\langle L_z^c \rangle$ and magnetization $\mathcal{M} = \int F_z dr$ vary as a function of the SOC strength λ, as exhibited in Fig. 2. We divide the SOC strength into eight regions, I–VIII, and different topological excitations in each region indicate that the ground state experiences phase transitions (for simplicity, we only exhibit the contour of $|\psi_{-2}|^2$). The density profile in region I exhibits a noncentrosymmetric distribution with no obvious vortex core, the density profile in region II exhibits an annulus distribution with a giant central hole, and an additional one to six small vortex cores around the central giant vortex core can be identified in regions III–VIII. Remarkably, $\langle L_z^c \rangle$ increases with λ while $\mathcal{M}$ decreases with λ within each region. With the variation from region I $\to$ region II, $\langle L_z^c \rangle$ and $\mathcal{M}$ change continuously, suggesting a second-order phase transition [36]. However, $\langle L_z^c \rangle$ and $\mathcal{M}$ change discontinuously during the transitions from region II $\to$ region III $\to \cdots \to$ region VIII, suggesting first-order phase transitions [36].

The aforementioned second-order phase transition (region I $\to$ region II) is further explained clearly in Fig. 3, where the rotation frequency is fixed at $\Omega = 0.25\omega_\perp$. Consistent with the one-dimensional (1D) density profile of the ψ_{-2} component, the condensate breaks the rotation symmetry when the SOC strength λ is increased from 0 to $0.025\omega_\perp\xi_0$. The position of the phase impurity (enclosed by the black rectangle) in the phase field $\arg(\psi_{-2})$ reveals that the vortex enters the condensate from the edge. With further increasing SOC strength λ, from $0.025\omega_\perp\xi_0 \to 0.05\omega_\perp\xi_0 \to 0.1\omega_\perp\xi_0$, the vortex gradually moves along the x direction and, finally, forms the central positioned vortex in region II. Considering the continuously changing canonical angular momentum $\langle L_z^c \rangle$ and magnetization $\mathcal{M}$ during the transition from region I to region II in Fig. 2, the condensate experiences a second-order phase transition.

C. Various topological excitations

We can gain further insight into the aforementioned topological excitations from the density distribution, phase field, spin vector, and velocity field. Two kinds of typical topological excitations in region II and region VI are illustrated in Fig. 4. When the rotation frequency $\Omega = 0.25\omega_\perp$ and the SOC strength $\lambda = 0.2\omega_\perp\xi_0$, the 2D and 1D density distributions of different components are exhibited in Figs. 4(a) and 4(b), respectively. The ψ_2 component is located at the center, which resembles a bright soliton with no density hole [37]. Additionally, the $\psi_{1,0,-1,-2}$ components exhibit a ring-shaped distribution with an expanded vortex core. The 1D density distribution of the topological excitation in region II is displayed in Fig. 4(b). The rotation symmetry of the total density is protected, the ψ_2 component dominates the central region, the ψ_{-2} component is located in the outside region, and the $\psi_{1,0,-1}$ components are sandwiched between the $\psi_{\pm 2}$ components.

The corresponding phase field $\arg(\psi_j)$ in Fig. 4(c) implies that the phase winding of the ψ_2 component is $\omega_2 = 0$, and the phase windings of the $\psi_{1,0,-1,-2}$ components are $\omega_1 = -1$,

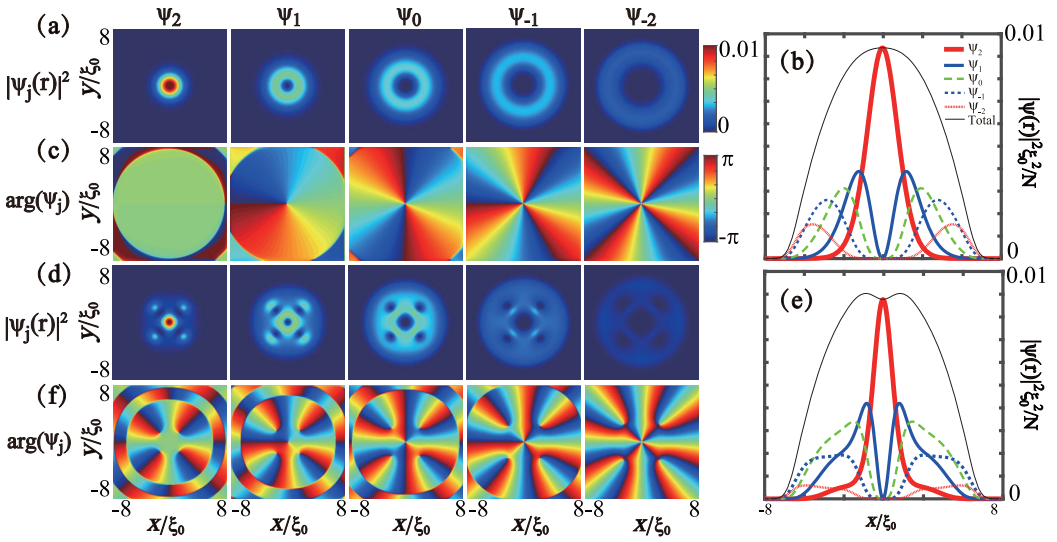

FIG. 4. The (a) 2D and (b) 1D density distributions of the ground state with the rotation frequency $\Omega = 0.25\omega_\perp$ and SOC strength $\lambda = 0.2\omega_\perp\xi_0$. (c) The corresponding phase fields for different components, where the phase windings for every component count $(\omega_2, \omega_1, \omega_0, \omega_{-1}, \omega_{-2}) = (0, -1, -2, -3, -4)$. The (d) 2D and (e) 1D density distributions of the ground state with $\Omega = 0.25\omega_\perp$ and $\lambda = 0.6\omega_\perp\xi_0$. (f) The corresponding phase fields for different components, where the phase windings for every component count $(\omega_2, \omega_1, \omega_0, \omega_{-1}, \omega_{-2}) = (-4, -5, -6, -7, -8)$.

$\omega_0 = -2$, $\omega_{-1} = -3$, and $\omega_{-2} = -4$, respectively. Apparently, the phase windings of the adjacent components differ by exactly 1. At rotation frequency $\Omega = 0.25\omega_\perp$ and SOC strength $\lambda = 0.6\omega_\perp\xi_0$, the 2D and 1D density distributions of different components are exhibited in Figs. 4(d) and 4(e), respectively. Compared to the Fig. 4(a) case, there are four additional density holes distributed around the trap center in Fig. 4(e), corresponding to four vortex cores. As shown in the 1D density distribution in Fig. 4(f), the ψ_2 component is still located in the central region where the $\psi_{1,0,-1,-2}$ components are at their minimum densities. The corresponding phase field $\arg(\psi_j)$ in Fig. 4(f) implies that the phase winding of the ψ_2 component is $\omega_2 = -4$, and the phase windings of the $\psi_{1,0,-1,-2}$ components are $\omega_1 = -5$, $\omega_0 = -6$, $\omega_{-1} = -7$, and $\omega_{-2} = -8$, respectively. Obviously, the phase winding of every component in the external four vortices equals 1, which differs from the centrally positioned vortex.

Nontrivial spin topological excitations, i.e., vortex and half-vortex, are particlelike topological structures in a continuous field that play a vital role in condensed matter physics. Spin topological excitations usually relate to various vortex structures [38]. Actually, the nontrivial topological excitation in region II suggests an Anderson-Toulouse vortex [39–41], as shown in the spin picture in Fig. 5(a). The detection of an AT vortex in spin-1/2 BECs has been realized by JILA [42] and in spin-1 or spin-2 BECs by MIT [43]. The spin densities are defined by $F_\mu = \sum_{m,n=0,\pm1,\pm2} \psi_m^\dagger(\hat{\sigma}_\mu)_{m,n}\psi_n/|\boldsymbol{\psi}|^2$, where $\mu = x, y, z$ and $\hat{\sigma}_\mu$ are spin-2 matrices [40,44]. Within the AT vortex, the positions of the phase windings in different components (except the ψ_2 component) are totally overlapped in the central region, with the spin vector pointing upward, which agrees well with the definition of the axisymmetric spin density F_z. Meanwhile, the spin aligns with a hyperbolic distribution that $(F_x, F_y) \propto (+y, -x)$, which is in good agreement with the AT vortex [45].

On the other hand, the spin texture of the nontrivial topological excitation in region VI is illustrated in Fig. 5(b). An AT vortex is still located in the center, while the peripheral four vortices exhibit different distributions in the spin image. Compared with the AT vortex, the positions of the phase windings in every component are separated. The phase windings of the $\psi_{1,2}$ components are located on one side of the ψ_0 component while the phase windings of the $\psi_{-1,-2}$ components are located on the other side, creating a vortex dipole [46]. Owing to the discrete distribution of different components, the spin densities F_x, F_y, and F_z of the vortex dipole (enclosed by the black square) are characterized by $(F_x, F_y, F_z) \propto (-x + y, -x + y, x + y)$, which differs from the AT vortex. When the rotation frequency is fixed, stronger SOC can further induce a vortex lattice with coaxially arranged annular arrays. In order to characterize the evolution of the vortex-dipole lattice, we define the layer numbers as a Mermin-Ho (MH) vortex as layer 1, an MH vortex and single-layer vortex dipole as layer 2, an MH vortex and two-layer vortex dipole as layer 3, and so on. As shown in Fig. 6(a) with the rotation frequency fixed at $\Omega = 0.1\omega_\perp$, $0.25\omega_\perp$, and $0.5\omega_\perp$, the layer number of vortex-dipole lattices increases with the SOC strength, which is different from the Abrikosov triangular lattice in superconductors [47] or hexagonal lattice in spinor BECs [48]. A three-layer vortex-dipole lattice is illustrated in Fig. 6(b), in which $\lambda = 1.4\omega_\perp\xi_0$ and $\Omega = 0.25\omega_\perp$. The particle current field is depicted as $J_c = \sum_j[\frac{\hbar}{2im}(\psi_j^\dagger\nabla\psi_j - \psi_j\nabla\psi_j^\dagger)]$, where $j = \pm2, \pm1, 0$ [31,32]. All the vortices share the same direction of circulation, which is different from the vortex-antivortex honeycomb lattices in spin-2 BECs [49]. Another key observation is that, in the case of strong SOC, $\lambda = 4\omega_\perp\xi_0$, we observed two perpendicular vortex chains, as depicted in Fig. 6(c). We can identify four plane waves in different quadrants from the canonical particle current field, and the directions of each plane wave are

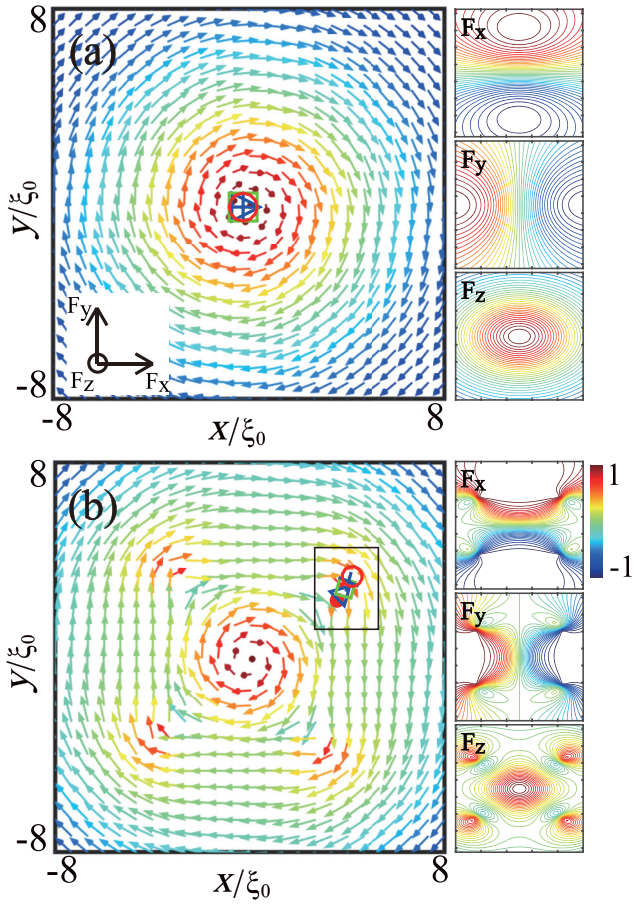

FIG. 5. (a) Spin vector and spin density (F_x, F_y, F_z) of the Mermin-Ho vortex when the rotation frequency $\Omega = 0.25\omega_\perp$ and the SOC strength $\lambda = 0.2\omega_\perp\xi_0$. The positions of phase winding in $(\psi_1, \psi_0, \psi_{-1}, \psi_{-2})$ are represented by (blue triangle, green square, blue cross, red circle). (b) Spin vector and spin density (F_x, F_y, F_z) of the vortex dipole when $\Omega = 0.25\omega_\perp$ and $\lambda = 0.6\omega_\perp\xi_0$. The positions of phase winding in $(\psi_2, \psi_1, \psi_0, \psi_{-1}, \psi_{-2})$ are represented by (red dot, blue triangle, green square, blue cross, red circle).

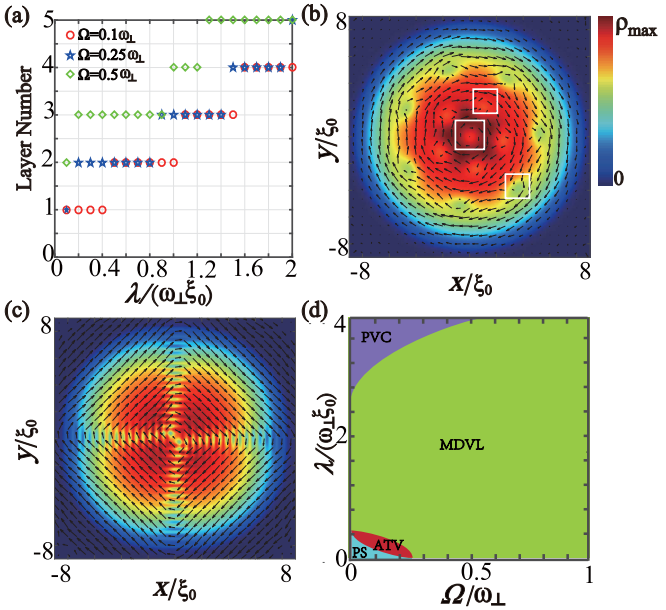

FIG. 6. (a) The layer number increases with the SOC when the rotation frequency $\Omega = 0.1\omega_\perp$, $\Omega = 0.25\omega_\perp$, and $\Omega = 0.5\omega_\perp$, respectively. (b), (c) Total density snapshots of a three-layer vortex-dipole lattice and perpendicular vortex chains with $\lambda = 1.4\omega_\perp\xi_0$ and $4\omega_\perp\xi_0$. Black arrows indicate the canonical current field. (d) Phase diagram of the ground states, including the phase separation (PS), the Anderson-Toulouse vortex (ATV), the multilayer vortex-dipole lattice (MDVL), and the perpendicular vortex chains (PVC).

perpendicular to each other. By projecting the propagating vector of one plane wave $\boldsymbol{k}$ onto the x and y directions, we note that the axial vortex chains are formed by two plane waves with opposite momenta, which is consistent with Ref. [24].

The ground-state diagram for spin-2 BECs has been reported with the single-condensate approximation [50] or within the cyclic phase [51]. The above-mentioned patterns can be classified into the λ-Ω phase diagram, as shown in Fig. 6(d). In the PS region, the ground states are formed by one plane wave propagating in a single direction. In the ATV region, the AT vortex dominates the trap center. In the MDVL region, a multilayer vortex-dipole lattice is introduced into the system. In the PVC region, two perpendicular vortex chains emerge.

D. Atomic-interaction-induced phase transition

To connect with experiments, atomic interactions concerning magnetic order should also be considered to trigger the topological vortical phase transition [17,52]. We hereby examine the influence of the spin-exchange interaction c_1/c_0 and spin singlet-pairing interaction c_2/c_0 on the phase transition in ferromagnetic spin-2 BECs [53,54]. Because the phase transition coexists with the canonical angular momentum evolution, we showcase the fitting curve of $\langle L_z^c\rangle$–c_1/c_0 in Fig. 7(a). Remarkably, $\langle L_z^c\rangle$ decreases when c_1/c_0 varies from −0.008 to −0.2 and the two-layer vortex-dipole lattice

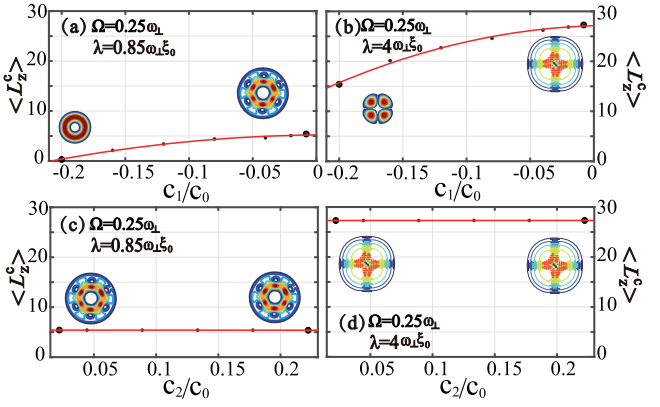

FIG. 7. (a), (b) Topological vortical phase transition spanned by the spin-exchange interaction c_1/c_0, where the rotation frequency $\Omega = 0.25\omega_\perp$, and the SOC strength $\lambda = 0.85\omega_\perp\xi_0$ in (a) and $\Omega = 0.25\omega_\perp$, $\lambda = 4\omega_\perp\xi_0$ in (b). (c), (d) Topological vortical phase transition spanned by the spin singlet-pairing interaction c_2/c_0, where $\Omega = 0.25\omega_\perp$, $\lambda = 0.85\omega_\perp\xi_0$ in (c) and $\Omega = 0.25\omega_\perp$, $\lambda = 4\omega_\perp\xi_0$ in (d).

gradually transforms into an AT vortex. However, as shown in Fig. 7(b), the perpendicular vortex chain structure is not influenced by the fluctuation (variation) of the spin-exchange interaction c_1/c_0, which indicates that strong SOC can protect topological excitation. On the other hand, when c_2/c_0 varies from 0.08 to 0.2, the $\langle L_z^c\rangle$–c_2/c_0 curve is flat in Figs. 7(c) and 7(d), which implies that the spin singlet-pairing interaction has little influence on the topological vortical phase transition.

E. Experimental implementation

We now report an experimental protocol to observe the aforementioned topological vortical phase transition. First, 4×10^5 ^{23}Na atoms are captured by laser-cooling in a pancake-shaped trap. The atomic scattering length is tuned by Feshbach resonance [55,56]. The choice of $a_4=43a_B$, $a_2=45.8a_B$, and $a_0=52.35a_B$ will lead to $c_0=201.36$, $c_1=-1.81$, and $c_2=24.15$, where a_B is the Bohr radius [57]. Using an off-resonant laser beam to provide a rotating gradient [42], BECs are stirred and possess an angular momentum with a certain frequency [58]. The system can be coupled by the laser beam when $\Omega=(0.25,0.5,1)\times\omega_\perp=2\pi\times(75,150,300)$ Hz are chosen. The pulsed magnetic fields are utilized to produce 2D Rashba SOC [59]. The phase transition versus the SOC strength is detected by plotting the $\langle\hat\sigma_z\rangle$-$\lambda$ curve, where the spin polarization $\langle\hat\sigma_z\rangle=\int\boldsymbol{\psi}^\dagger\hat\sigma_z\boldsymbol{\psi}$. At the phase boundary, $\langle\hat\sigma_z\rangle$ experiences a discontinuous jump, which indicates a first-order phase transition [60].

IV. CONCLUSION

In conclusion, we have studied the topological vortical phase transition of spin-2 BECs under the combination of Rashba-type SOC and rotation. The phase transition among a vortex-dipole lattice, perpendicular vortex chains, and an AT vortex can be well controlled via manipulation of SOC. We fully illuminate the first-order and the second-order phase transitions according to the continuous and discontinuous behaviors of the canonical angular momentum or magnetization. Furthermore, when facing SOC and rotation, the spin-exchange interaction can also trigger the phase transition while the spin singlet-pairing interaction has little effect on it. Our results will guide further experimental and theoretical work on the intriguing property of the topological vortical phase transition in quantum many-body systems.

ACKNOWLEDGMENTS

We acknowledge helpful discussions with J. Li, W. Han, and J. Jin. This work was supported by the National Key R & D Program of China under Grant No. 2016YFA0301500, the Natural Science Foundation of China under Grants No. 61835013, No. 11971067, No. 11875149, and No. 61565007, the Strategic Priority Research Program of the Chinese Academy of Sciences under Grants No. XDB01020300 and No. XDB21030300, Fundamental Research Funds for the Central Universities under Grant No. 2020NTST22, the Youth Jinggang Scholars Program in Jiangxi Province, and The Program of Qingjiang Excellent Young Talents, Jiangxi University of Science and Technology.

APPENDIX: GROSS-PITAEVSKII EQUATIONS FOR SPIN-2 BECs

Here we discuss in detail how the full three-dimensional (3D) Gross-Pitaevskii equations transform into the two-dimensional (2D) form mentioned in the text. The coupled 3D Gross-Pitaevskii equations can be cast into a dimensionless form by scaling the spatial coordinates as $\tilde x=x/\xi_0$, $\tilde y=y/\xi_0$, and $\tilde z=z/\xi_0$, the time as $\tilde t=t\omega_\perp$, and the wave function as $\tilde\psi_j(\tilde x,\tilde y,\tilde z,\tilde t)=\sqrt{\xi_0^2/N_j}\psi_j(x,y,z,t)$. Here, the index $j=\pm2,\pm1,0$ refers to each of the species of the five-component BEC, while $\xi_0=\sqrt{\hbar/m\omega_\perp}$ is the harmonic oscillator length. For simplicity, it is convenient to drop the tilde and require that the trapping frequency in the transverse x-y plane satisfies $\omega_2=\omega_1=\omega_0=\omega_{-1}=\omega_{-2}=\omega_\perp$. The quasi-2D harmonic trap is achieved via maneuvering much stronger trapping in the axial z direction compared to that along the x-y plane, i.e., $\omega_z\gg\omega_\perp$. Along this line, $\omega_z/\omega_\perp\gg1$, the wave function of each species can be characterized as

$$\psi_j(x,y,z,t)=\psi_j(x,y,t)\phi_j(z), \tag{A1}$$

where $\phi_j(z)$ is the normalized ground-state wave function in the z direction. Subsequently, the dimensionless forms of the coupled Gross-Pitaevskii equations after integrating over $\phi_j(z)$ lead to the 2D forms [26,27,29,30],

$$\begin{aligned}i\frac{\partial\psi_{\pm2}(x,y,t)}{\partial t}&=h\psi_{\pm2}(x,y,t)+c_0\rho\psi_{\pm2}(x,y,t)\\&+c_1(F_\mp\psi_{\pm1}(x,y,t)\pm2F_z\psi_{\pm2}(x,y,t))\\&+\frac{c_2}{\sqrt5}\Theta\psi_{\mp2}(x,y,t)^\dagger\\&+\lambda(-i\partial x\mp\partial y)\psi_{\pm1}(x,y,t)\\&+i\Omega(x\partial y-y\partial x)\psi_{\pm2}(x,y,t),\end{aligned} \tag{A2}$$

$$\begin{aligned}i\frac{\partial\psi_{\pm1}(x,y,t)}{\partial t}&=h\psi_{\pm1}(x,y,t)+c_0\rho\psi_{\pm1}(x,y,t)\\&+c_1\left(\frac{\sqrt6}{2}F_\mp\psi_0(x,y,t)+F_\pm\psi_{\pm2}(x,y,t)\right.\\&\left.\pm F_z\psi_{\pm1}(x,y,t)\right)-\frac{c_2}{\sqrt5}\Theta\psi_{\mp1}(x,y,t)^\dagger\\&+\lambda(-i\partial x\pm\partial y)\psi_{\pm2}(x,y,t)\\&+\lambda\left(-i\frac{\sqrt6}{2}\partial x\mp\frac{\sqrt6}{2}\partial y\right)\psi_0(x,y,t)\\&+i\Omega(x\partial y-y\partial x)\psi_{\pm1}(x,y,t),\end{aligned} \tag{A3}$$

$$\begin{aligned}i\frac{\partial\psi_0(x,y,t)}{\partial t}&=h\psi_0(x,y,t)+c_0\rho\psi_0(x,y,t)\\&+\frac{\sqrt6}{2}c_1(F_-\psi_{-1}(x,y,t)+F_+\psi_1(x,y,t))\\&+\frac{c_2}{\sqrt5}\Theta\psi_0(x,y,t)^\dagger\\&+\lambda\left(-i\frac{\sqrt6}{2}\partial x+\frac{\sqrt6}{2}\partial y\right)\psi_1(x,y,t)\end{aligned}$$

$$+\lambda\left(-i\frac{\sqrt{6}}{2}\partial x-\frac{\sqrt{6}}{2}\partial y\right)\psi_{-1}(x,y,t)$$
$$+i\Omega(x\partial y-y\partial x)\psi_0(x,y,t), \tag{A4}$$

where $h=-\frac{1}{2}(\partial_x^2+\partial_y^2)+\frac{1}{2}(x^2+y^2)$. Moreover,

$$F_+ = F_-{}^\dagger$$
$$= 2(\psi_{-1}(x,y,t)^\dagger\psi_{-2}(x,y,t)+\psi_2(x,y,t)^\dagger\psi_1(x,y,t))$$
$$+\sqrt{6}(\psi_1(x,y,t)^\dagger\psi_0(x,y,t)+\psi_0(x,y,t)^\dagger\psi_1(x,y,t)),$$

$$F_z = 2|\psi_2(x,y)|^2+|\psi_1(x,y)|^2-|\psi_{-1}(x,y)|^2-2|\psi_{-2}(x,y)|^2,$$

and

$$\Theta=[2\psi_2(x,y,t)\psi_{-2}(x,y,t)-2\psi_1(x,y,t)\psi_{-1}(x,y,t)$$
$$+\psi_0(x,y,t)^2]/\sqrt{5}.$$

We can define the dimensionless strength of SOC as $\lambda/\sqrt{\frac{\hbar\omega_\perp}{m}}=\lambda/(\omega_\perp\xi_0)$ and the dimensionless rotation frequency as $\Omega/\omega_\perp$. In our numerical simulations, the size of the computational grid is 300×300, corresponding to a field of view of 30×30 $(\xi_0{}^2)$. We choose general Gaussian wave functions for the five components as the initial states. A sufficiently large number of time steps to guarantee that we obtain the ground states is chosen. The imaginary-time propagation starts with a Gaussian initial state in each component: $\psi_j\sim\exp(-(x^2+y^2)/\alpha_j)$, where α_j is the width.

[1] W. Choi, K. H. Lee, and Y. B. Kim, Phys. Rev. Lett. **124**, 117205 (2020).
[2] Y. Lu, W.-Y. He, D.-H. Xu, N. Lin, and K. T. Law, Phys. Rev. B **94**, 024507 (2016).
[3] I. Andrade, D. Bazeia, M. A. Marques, and R. Menezes, Phys. Rev. D **102**, 025017 (2020).
[4] H. Edri, B. Raz, N. Matzliah, N. Davidson, and R. Ozeri, Phys. Rev. Lett. **124**, 163401 (2020).
[5] A. Tononi and L. Salasnich, Phys. Rev. Lett. **123**, 160403 (2019).
[6] C. Hamner, Y. Zhang, J. J. Chang, C. Zhang, and P. Engels, Phys. Rev. Lett. **111**, 264101 (2013).
[7] Y. V. Kartashov, B. A. Malomed, Y. Shnir, and L. Torner, Phys. Rev. Lett. **113**, 264101 (2014).
[8] C. C. Bradley, C. A. Sackett, J. J. Tollett, and R. G. Hulet, Phys. Rev. Lett. **75**, 1687 (1995).
[9] K. B. Davis, M. O. Mewes, M. R. Andrews, N. J. van Druten, D. S. Durfee, D. M. Kurn, and W. Ketterle, Phys. Rev. Lett. **75**, 3969 (1995).
[10] C. Lobo, A. Sinatra, and Y. Castin, Phys. Rev. Lett. **92**, 020403 (2004).
[11] A.-C. Ji, W. M. Liu, J. L. Song, and F. Zhou, Phys. Rev. Lett. **101**, 010402 (2008).
[12] V. Baltz, A. Manchon, M. Tsoi, T. Moriyama, T. Ono, and Y. Tserkovnyak, Rev. Mod. Phys. **90**, 015005 (2018).
[13] T. Chiba and T. Komine, Phys. Rev. Applied **14**, 034031 (2020).
[14] Y.-J. Lin, K. Jimeńez-Garcia, and I. B. Spielman, Nature **471**, 83 (2011).
[15] R. Liao, Phys. Rev. Lett. **120**, 140403 (2018).
[16] M. Iskin and A. L. Subaşi, Phys. Rev. A **87**, 063627 (2013).
[17] C. Wang, C. Gao, C.-M. Jian, and H. Zhai, Phys. Rev. Lett. **105**, 160403 (2010).
[18] S.-W. Su, S.-C. Gou, Q. Sun, L. Wen, W.-M. Liu, A.-C. Ji, J. Ruseckas, and G. Juzeliūnas, Phys. Rev. A **93**, 053630 (2016).
[19] Q.-Q. Lü and D. E. Sheehy, Phys. Rev. A **88**, 043645 (2013).
[20] E. V. Shuryak, Phys. Rev. A **54**, 3151 (1996).
[21] E. Lundh, Phys. Rev. A **65**, 043604 (2002).
[22] X.-F. Zhou, J. Zhou, and C. Wu, Phys. Rev. A **84**, 063624 (2011).
[23] J. Jin, W. Han, and S. Zhang, Phys. Rev. A **98**, 063607 (2018).
[24] X.-Q. Xu and J. H. Han, Phys. Rev. Lett. **107**, 200401 (2011).
[25] H. Takeuchi, Phys. Rev. Lett. **126**, 195302 (2021).
[26] H. Saito and M. Ueda, Phys. Rev. A **72**, 053628 (2005).
[27] Z. F. Xu, R. Lü, and L. You, Phys. Rev. A **83**, 053602 (2011).
[28] D. Baye and J.-M. Sparenberg, Phys. Rev. E **82**, 056701 (2010).
[29] W. V. Pogosov, R. Kawate, T. Mizushima, and K. Machida, Phys. Rev. A **72**, 063605 (2005).
[30] G.-P. Zheng, Y.-G. Tong, and F.-L. Wang, Phys. Rev. A **81**, 063633 (2010).
[31] X.-Q. Xu and J. H. Han, Phys. Rev. Lett. **108**, 185301 (2012).
[32] C. Qu and S. Stringari, Phys. Rev. Lett. **120**, 183202 (2018).
[33] A. L. Fetter, Rev. Mod. Phys. **81**, 647 (2009).
[34] M. Tsubota, K. Kasamatsu, and M. Ueda, Phys. Rev. A **65**, 023603 (2002).
[35] K. Kasamatsu, M. Tsubota, and M. Ueda, Phys. Rev. A **67**, 033610 (2003).
[36] G. M. Kavoulakis, B. Mottelson, and C. J. Pethick, Phys. Rev. A **62**, 063605 (2000).
[37] D. Ma and C. Jia, Phys. Rev. A **100**, 023629 (2019).
[38] C.-F. Liu, H. Fan, Y.-C. Zhang, D.-S. Wang, and W.-M. Liu, Phys. Rev. A **86**, 053616 (2012).
[39] T. Mizushima, K. Machida, and T. Kita, Phys. Rev. Lett. **89**, 030401 (2002).
[40] T. Mizushima, N. Kobayashi, and K. Machida, Phys. Rev. A **70**, 043613 (2004).
[41] J.-P. Martikainen, A. Collin, and K.-A. Suominen, Phys. Rev. A **66**, 053604 (2002).
[42] M. R. Matthews, B. P. Anderson, P. C. Haljan, D. S. Hall, C. E. Wieman, and E. A. Cornell, Phys. Rev. Lett. **83**, 2498 (1999).
[43] A. E. Leanhardt, Y. Shin, D. Kielpinski, D. E. Pritchard, and W. Ketterle, Phys. Rev. Lett. **90**, 140403 (2003).
[44] K. Kasamatsu, M. Tsubota, and M. Ueda, Phys. Rev. Lett. **93**, 250406 (2004).
[45] K. Kasamatsu, M. Tsubota, and M. Ueda, Phys. Rev. A **71**, 043611 (2005).
[46] C.-F. Liu and W. M. Liu, Phys. Rev. A **86**, 033602 (2012).
[47] W. H. Kleiner, L. M. Roth, and S. H. Autler, Phys. Rev. **133**, A1226 (1964).
[48] S.-W. Su, C.-H. Hsueh, I.-K. Liu, T.-L. Horng, Y.-C. Tsai, S.-C. Gou, and W. M. Liu, Phys. Rev. A **84**, 023601 (2011).
[49] T. Mawson, G. Ruben, and T. Simula, Phys. Rev. A **91**, 063630 (2015).

[50] C. V. Ciobanu, S.-K. Yip, and T.-L. Ho, Phys. Rev. A **61**, 033607 (2000).
[51] T. Kawakami, T. Mizushima, and K. Machida, Phys. Rev. A **84**, 011607(R) (2011).
[52] D. M. Stamper-Kurn and M. Ueda, Rev. Mod. Phys. **85**, 1191 (2013).
[53] M. Ueda and M. Koashi, Phys. Rev. A **65**, 063602 (2002).
[54] S. Gautam and S. K. Adhikari, Phys. Rev. A **91**, 013624 (2015).
[55] J. L. Roberts, N. R. Claussen, J. P. Burke, C. H. Greene, E. A. Cornell, and C. E. Wieman, Phys. Rev. Lett. **81**, 5109 (1998).
[56] A. Griesmaier, J. Werner, S. Hensler, J. Stuhler, and T. Pfau, Phys. Rev. Lett. **94**, 160401 (2005).
[57] J. Han and M. Tsubota, Phys. Rev. A **99**, 033607 (2019).
[58] K. W. Madison, F. Chevy, W. Wohlleben, and J. Dalibard, Phys. Rev. Lett. **84**, 806 (2000).
[59] Z. Wu, L. Zhang, W. Sun, X.-T. Xu, B.-Z. Wang, S.-C. Ji, Y. Deng, S. Chen, X.-J. Liu, and J.-W. Pan, Science **354**, 6308 (2016).
[60] D. Zhang, T. Gao, P. Zou, L. Kong, R. Li, X. Shen, X.-L. Chen, S.-G. Peng, M. Zhan, H. Pu, and K. Jiang, Phys. Rev. Lett. **122**, 110402 (2019).